Non-Intrusive and Precise Electric Field Sensing of High-Field Electron Devices by Franz-Keldysh Effect

Xinyi Pei[1#], Hehe Gong[2#], Na Sun[1], Songhao Gu[1], Jianhong Zhang[1], Zesen Liu[1], Fang-Fang Ren[1], Binggege Guo[2],
Dawei Yan[3], Hai Lu[1], Shulin Gu[1], Xinran Wang[1], Rong Zhang[1], Xiaoting Jia[2*], Yuhao Zhang[2*], Jiandong Ye[1*]

[1] School of Electronic Science and Engineering, Nanjing University, Nanjing, China. [2] The Bradley Department of Electrical and Computer Engineering, Virginia Tech, Blacksburg, VA USA. [3] School of Integrated Circuits, Jiangnan University, Wuxi, China
[#]These two authors contributed equally to this work. *Emails: xjia@vt.edu, yhzhang@vt.edu, and yejd@nju.edu.cn

Abstract—Precise sensing of electric fields (*E*-fields) inside a device region is crucial for condition monitoring and structural optimization of optoelectronic and electron devices. However, this is challenging for wide- and ultra-wide bandgap (UWBG) semiconductor devices, due to the high internal *E*-field up to several MV/cm. Moreover, current *E*-field sensing techniques are often surface sensitive, intrusive, or material specific. Here, we demonstrate a precise and noninvasive method based on the Franz-Keldysh (F-K) effect to sense the internal *E*-field in operating high-voltage devices. This method can also map the 2-D spatial distribution of *E*-field with a sub-micrometer (µm) resolution. To illustrate the capabilities of this method, we use it to map the *E*-field in three UWBG gallium oxide (Ga_2O_3) diodes with only small variation in contact or edge termination. Our measurements reveal very different *E*-field distributions in these devices, which underpin the physics causing their large differences in breakdown voltage. These *E*-field distributions are validated by device simulations and emission microscopy. To date, this is the first demonstration of *E*-field mapping in UWBG devices, and the max detection strength (3.1 MV/cm) is the highest reported in all *E*-field sensing techniques. This method also has a wide applicability due to the common existence of F-K effect in nearly all bulk semiconductors.

I. INTRODUCTION

E-field determines the carrier transport and device function. It is also a key precursor of device degradation. Hence, *E*-field sensing is highly desirable for device condition monitoring and structural optimization. However, precise *E*-field sensing has long been a challenge for operating semiconductor devices. Engineers often rely on the technology computer-aided design (TCAD) simulations to predict *E*-field distributions inside a device, but their experimental validation is usually lacking.

To date, several techniques have been reported for *E*-field sensing in devices. The optically based techniques offer non-contact and direct *E*-field mapping, but are often sensitive to surface properties and only applicable to specific materials. For example, electroreflectance and photoreflectance have been used for GaN devices but are unsuitable at high *E*-fields due to the severe reflectance oscillations decay [1]. Atomic-scale sensing of *E*-field in diamond relies on the unique spin property of nitrogen vacancies (NVs) [2]. However, fabrication of NV centers requires ion implantation and causes intrusive changes to device structure. Recently, Electric-field-induced second harmonic generation (EFISHG) is used to map *E*-fields up to 2 MV/cm in GaN devices [3], but its applicability is limited by the nonlinear susceptibility and material symmetry.

The Franz-Keldysh effect contains the change in optical absorption by a semiconductor under an *E*-field. Wavefunctions of electrons and holes leak into the bandgap with damping, enabling electrons to tunnel into the conduction band (Fig. 1). This effect is common to all bulk semiconductors and underpins the electro-absorption modulators, which tunes optical power by changing the absorption edge at high speeds with tens of GHz bandwidth. Conversely, the F-K effect can determine the *E*-field by detecting the absorption edge shift, especially in high-field devices. Pioneer work using F-K effect has been conducted in GaN and SiC, but the measurements are limited by opaque contacts and only detect an average *E*-field instead of a spatial mapping [4, 5]. It is unknown if the F-K effect can be applied to UWBG devices and for *E*-field mapping.

This work, for the first time, demonstrates a noninvasive *in-situ* sensing technique to precisely map the local *E*-fields in operating UWBG high-field devices through rigorous modeling of F-K sub-gap photoresponse features, achieving a detection range up to 3.1 MV/cm. The sub-µm -resolved mapping of field inhomogeneities allows for the physical understanding of breakdown voltage and the precise identification of failure spots in operating high-field devices, offering direct guidelines for optimizing device performance and reliability.

II. DEVICE DESIGN, FAB, AND CHARACTERISTICS

To illustrate the capabilities of the proposed method, we apply it to UWBG Ga_2O_3 devices, which are under intensive research for power, RF, memory, digital, and optoelectronic applications. Three Ga_2O_3 diodes are fabricated on the same wafer with differences only in the contact and edge termination. One diode is a Schottky barrier diode (SBD), and the other two are p-n diodes (PNDs) with a thin (5 nm) p-type NiO between n-Ga_2O_3 and anode (Fig. 2). In one PND (PND-1), the NiO edge aligns with the anode edge. In the other PND (PND-2), the NiO edge extends 10-µm beyond the anode edge.

The device fabrication started from the Ga_2O_3 wafer that comprises an 8-µm β-Ga_2O_3 layer (N_d=2×10^{16} cm^{-3}) on a conductive Ga_2O_3 substrate. Ti/Au is used for back-side Ohmic contact. A semitransparent electrode (5 nm Ni) is the Schottky contact in SBD. For PND-1, a 5 nm p-type NiO (N_a=5×10^{18} cm^{-3}) was deposited by RF magnetron sputtering followed by a 5 nm Ni deposition. For PND-2, only 5 nm NiO was deposited. Finally, both SBD and PND underwent a 200 nm Au deposition as the central anode with an active area of 0.16 mm^2.

2024 IEEE International Electron Devices Meeting (IEDM) | 979-8-3503-6542-9/24/$31.00 ©2024 IEEE | DOI: 10.1109/IEDM50854.2024.10873542

Fig. 3 shows the forward and reverse *I-V* characteristics of the three devices. Their breakdown voltages (*BV*s) show a large difference. The *BV* of PND-2 (1.52 kV) is nearly twice of the SBD's *BV* (0.82 kV). The PND-1 and PND-2 show almost identical forward *I-V* curves but a nearly 50% difference in *BV*. Such large *BV* difference, despite small structure variations, suggest the need to understand the E-field distributions.

III. MODELING AND IN-SITU SENSING OF *E*-FIELD

Near-band-edge photoresponse modeling. β-Ga_2O_3 has an indirect band transition with a large exciton binding energy (E_X^0=230 meV). Therefore, the F-K effect is modeled in the framework of Merkulov theory, which considers the electro-absorption of Wannier-Mott exciton [6]. The field-dependent near-band-edge absorption coefficient α is given as

$$\alpha[E(z),E_{ph}] = Cx/\pi^2(\delta^2 x^2+1) \qquad (1)$$

where C is the exciton wavefunction normalization coefficient, and x is the correction due to the potential barrier lowering as a result of the exciton Coulomb interaction. Table I lists the definition of other key parameters, including the exciton photon energy deficit Δ and the exciton Bohr radius a_B (0.7 nm for Ga_2O_3) [7]. The vertical *E*-field, $E(z)$, follows a triangular distribution, i.e., $E(z)=E_{\max}(1\text{-}z/W_n)$, where $E_{\max}$ is the max E-field at junction interfaces that primarily determines the device.

As shown in Fig. 4, light illuminating from the top electrode (Φ_0) experiences three main attenuation processes: 1) reflection and absorption by the semitransparent layer, resulting in photon flux Φ_{out1}; 2) absorption in the depletion region and the minority carrier diffusion region, leaving photon flux Φ_{out2}; 3) absorption in the field-free region and substrate. The 2) is dominant. The 3) is negligible due to the minimal sub-bandgap absorption coefficient (<1000 cm^{-1}) [9]. Thus, the effective absorption is

$$\Phi_{absorb} = \Phi_{out1} - \Phi_{out2} = \Phi_{out1}\left(1 - e^{-\int_0^{W_n}\alpha[E(z),E_{ph}]dz}\right) \qquad (2)$$

Considering the different device architectures, the depth-dependent responsivity of SBD and PNDs are listed in Table II.

Photoresponse measurement and fitting. The photocurrent spectroscopy setup is shown in Fig. 5, which enables *in-situ* measurements of the photoresponse from operating devices under biases up to 200 V, with a sub-μm spatial resolution. The photoresponse spectra of all three devices showcase obvious broadening and redshift of absorption edges induced by F-K effect with increasing reverse biases (Fig. 6). These spectra are quantitatively fitted to an exciton F-K model over a broad photon energy range (Fig. 7) using a single fit parameter $E_{\max}$. Based on the key modeling parameters as listed in Table III, the spectrally determined magnitudes of $E_{\max}$ vary almost linearly with the applied bias (V_{bias}) for all devices. Compared to the interface *E*-field extracted by TCAD simulation (Fig. 8a), the quantified $E_{\max}$ of SBD and PND-1 matches well, while that of PND-2 are slightly higher. This discrepancy is attributed to the high resistivity of NiO, leading to more lateral voltage drop near the central electrode, which is not accounted in the simulation.

IV. E-FIELD MAPPING AND PHYSICAL UNDERSTANDING

The above quantitative fitting allows for building the direct relationship between $E_{\max}$ and photoresponse intensity (Fig. 8b). Both PNDs show a linear relationship between the photocurrent and $E_{\max}$, while SBD shows an exponential relationship given the self-trapped-hole-induced barrier-lowering effect.

Fig. 9a shows the photocurrent mapping results of three devices under different reverse biases up to 200 V with a sub-μm resolution. The maximum photocurrent is located near the electrode edges for all devices, while the distribution in PND-2 is the most spreading out spatially. Fig. 9b shows the *E*-field distributions derived from the photocurrent, confirming the more even distribution in PND-2. TCAD simulations are then performed for validation (Fig. 10a). Fig. 10b compares the extracted and simulated *E*-fields along the cutline shown in Fig. 9 for three devices at various V_{bias}, revealing a good consistency with *E*-field strength up to 3.1 MV/cm. The small discrepancy in PND-2 is due to the aforementioned lateral bias in p-NiO.

The E-field mapping reveals the key physics behind the higher *BV* in PND-2 as compared to PND-1. With a merely 10-μm difference in the NiO extension length, the internal *E*-field changes dramatically, and the peak *E*-field moves from the NiO edge to the anode edge in PND-2 (see Figs. 9-10). The NiO extension is fully depleted, effectively spreading the crowded *E*-field and reducing the peak *E*-field. To experimentally verify this mechanism, we perform the Emission Microscopy (EMMI) characterization of three devices at their respective *BV*, which allows for visualizing the killing leakage current spot at *BV*. As shown in Fig. 11, the failure spots in SBD and PND-1 are both at the device edge, while that in PND-2 moves from the NiO edge to the anode edge, which are consistent with the peak *E*-field locations from the mapping. This shows the capability of the *in-operanto* *E*-field mapping at a lower bias to predict the device destructive failure location in overvoltage conditions.

V. BENCHMARK AND CONCLUSION

Table IV benchmarks the mechanism, performance and applicability of our F-K effect-based method with other *E*-field sensing methods reported previously [1-3, 10-12]. Our method highlights the concurrent realization of the noninvasive sensing of operating devices and the sub-μm resolution mapping, as well as the highest *E*-field strength (3.1 MV/cm) reported in all methods and the first application to UWBG devices. Beyond the advance in the sensing method, the *E*-field distributions measured in three Ga_2O_3 diodes reveal key understanding on their *BV*, particularly 'visualizing' the functionality of the NiO extension in *E*-field modulation which has not been reported before. Considering the common existence of F-K effect, this method can be applied to numerous semiconductor devices to facilitate improvement of their performance and reliability.

Acknowledgement: The NJU authors acknowledge the funding support by the National Key R&D Program of China (2022YFB3605403), NSFC (62234007, 62293521, U21A20503, and U21A2071). The VT authors acknowledge the support from NSF (ECCS-2230412).

REFERENCES

[1] L. Janicki *et al., Appl. Phys. Lett.,* vol. 113, pp. 032109, 2018.
[2] T. Iwasaki *et al.*, *ACS Nano.*, vol. 11, pp. 1238, 2017.
[3] Y. K. Cao *et al.*, *Nat. Electron.*, vol. 4, pp. 478-485, 2021.
[4] T. Maeda *et al.*, *Appl. Phys. Express.,* vol. 112, pp. 252104, 2018.
[5] D. Verma *et al.*, *Appl. Phys. Lett.*, vol. 116, pp. 202102, 2020.
[6] I. A. Merkulov, *Sov. Phys. Semicond.,* vol. 39, pp. 2314, 1974.
[7] M. M. R. Adnan, *et al. Phys. Rev. Appl*., vol. 16, pp. 034011, 2021.
[8] R. Newman and R. M. Chrenko, *Phys. Rev.* vol. 114, pp. 1507, 1959.
[9] H. Peelaers, *et al. Appl. Phys. Lett*., vol. 111, pp. 182104, 2017.
[10] K. Nakagami *et al.*, *Appl. Phys. Lett*., vol. 85, pp. 6028, 2004.
[11] J. Möreke *et al.*, *Microelectron Reliab*., vol. 54, pp. 921, 2014.
[12] S. Rajasingam *et al.*, *IEEE Electron Device Lett.*, vol. 25, pp. 456, 2004.

Franz-Keldysh Effect and High-field Devices Characteristics

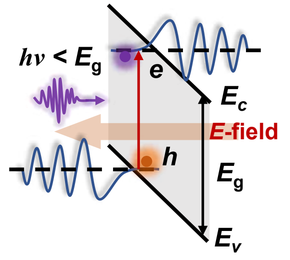

$$\alpha[E(z),E_{ph}]=Cx/\pi^2(\delta^2x^2+1)$$

Fig. 1. Principle of the Franz-Keldysh effect in a semiconductor under electric field and light illumination.

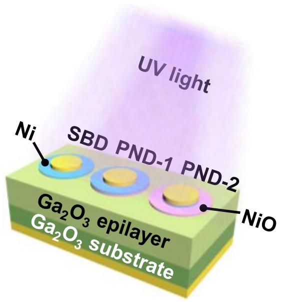

Fig. 2. Schematic diagram of the fabricated three β-Ga_2O_3 diodes investigated in this work.

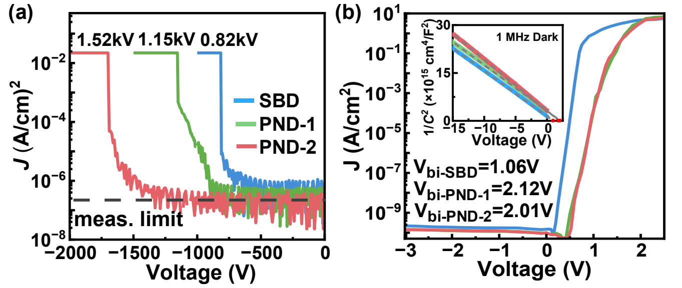

Fig. 3. (a) Reverse and (b) forward *I-V* characteristics of the three devices and the inset of (b) is the *C-V* plots used to extract the built-in potential (V_{bi}) of each device. The difference in forward *I-V* of PND and SBD is due to V_{bi} distinction.

Sub-gap Photoresponse (PR) and F-K Effect Modeling

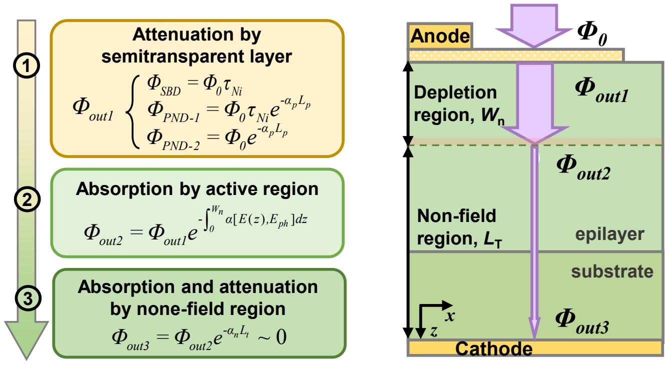

① **Attenuation by semitransparent layer**

$$\Phi_{out1}\begin{cases}\Phi_{SBD}=\Phi_0\tau_{Ni}\\ \Phi_{PND\text{-}1}=\Phi_0\tau_{Ni}e^{-\alpha_pL_p}\\ \Phi_{PND\text{-}2}=\Phi_0e^{-\alpha_pL_p}\end{cases}$$

② **Absorption by active region**

$$\Phi_{out2}=\Phi_{out1}e^{-\int_0^{W_n}\alpha[E(z),E_{ph}]dz}$$

③ **Absorption and attenuation by none-field region**

$$\Phi_{out3}=\Phi_{out2}e^{-\alpha_nL_t}\sim 0$$

Fig. 4. Schematic diagram of the light transmission process within the devices and the attenuation of light in each region.

Table I. Equations of the field-dependent exciton F-K effect.

$\alpha[E(z),E_{ph}]=\dfrac{Cx}{\pi^2(\delta^2x^2+1)}$	(1)	$x=\dfrac{8}{f}exp[-\dfrac{4}{3}\dfrac{\Delta^{3/2}}{f}-\dfrac{2}{\sqrt{\Delta}}ln(8\dfrac{\Delta^{3/2}}{f})]$	(2)
$\delta=\Delta-1-9f^2/2$	(3)	$\Delta=\lvert E_g-E_{ph}\rvert/E_X$	(4)
$f=ea_BE(z)/E_X$	(5)	$E_X=E_X^0+E(z)^2\,9e^2a_B{}^2/8E_X^0$	(6)

Table II. The photoresponsivity equation of the three devices.

Photoresponsivity	$R_{ph}=I_{ph}/P_{opt}A_{eff}=\eta e\Phi_{absorb}/\Phi_0E_{ph}$	(7)
SBD	$R_{ph\text{-}SBD}=e\eta\tau_{Ni}[1-exp(-\int_0^{W_n}\alpha[E(z),E_{ph}]dz)]/E_{ph}$	(8)
PND-1	$R_{ph\text{-}PND\text{-}1}=e\eta\tau_{Ni}exp(-\alpha_pL_p)[1-exp(-\int_0^{W_n}\alpha[E(z),E_{ph}]dz)]/E_{ph}$	(9)
PND-2	$R_{ph\text{-}PND\text{-}2}=e\eta exp(-\alpha_pL_p)[1-exp(-\int_0^{W_n}\alpha[E(z),E_{ph}]dz)]/E_{ph}$	(10)

Table III. Parameters in the photoresponse models and spectra fitting.

Parameter	Symbol	Value	Unit
Light energy	E_{ph}	1240/λ	eV
Light power density	P_{opt}	$I_{Si}/R_{Si}A_{Si}$	W/mm^2
Effective illumination area	A_{eff}	0.07	mm^2
Internal quantum efficiency	η	~ 1	-
Transmissivity of 5 nm Ni	τ_{Ni}	0.75	-
Absorption coefficient of NiO	α_p	4×10^5 [8]	cm^{-1}
Thickness of NiO	L_p	5	nm
Vertical *E*-field in Ga_2O_3	$E(z)$	$E(z)=E_{max}(1-z/W_n)$	MV/cm
Depletion width in Ga_2O_3	W_n	$W_n=(\varphi_{bi}+\lvert V_{bias}\rvert)/E_{max}$	nm
Built-in potential	φ_{bi}	1.06 for SBD 2.12 for PND-1 2.01 for PND-2	eV

W_n for PND: $\varphi_{bn}+\lvert V_{bn}\rvert=[N_A\varepsilon_p/(N_A\varepsilon_p+N_D\varepsilon_n)](\varphi_{bi}+\lvert V_{bias}\rvert)$, ε_p=9.1 and ε_n=10.2 is the relative dielectric constant of NiO and Ga_2O_3, respectively.

PR Spectroscopy Setup and Quantitative Fitting

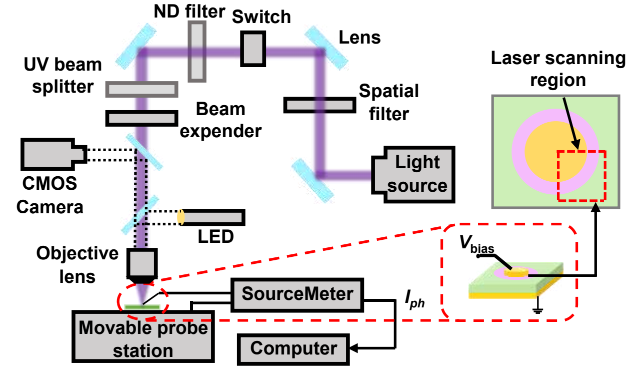

Fig. 5. Schematic diagram of the optical system for the photoresponse spectra and scanning photocurrent spectra characterizations.

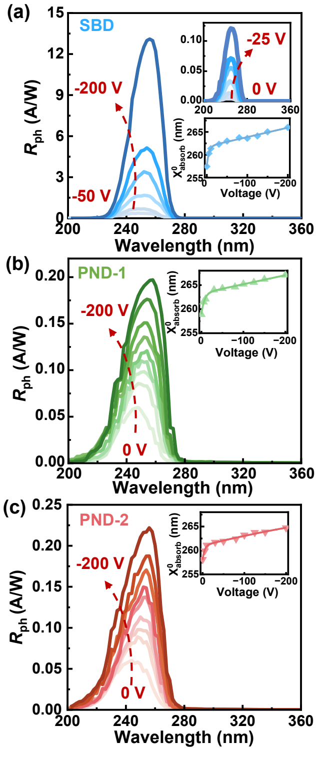

Fig. 6. Photoresponse spectra as a function of light wavelength for three devices at various biases. The insets show absorption edge redshift *vs.* bias.

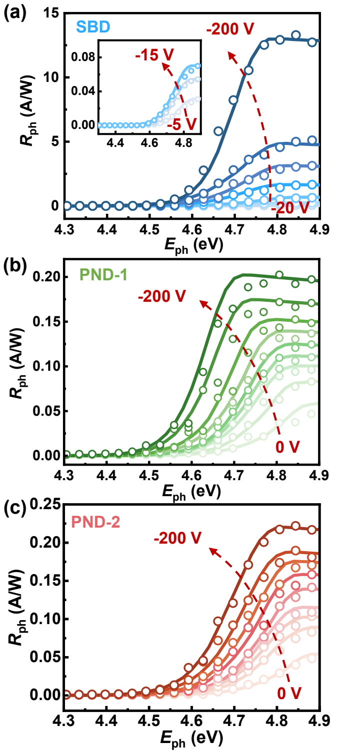

Fig. 7. Fitting results from equations in Table II with respect to the experimental photoresponsivity data as a function of incident photon energy (E_{ph}) with bias.

Two-dimensional *E*-Field Mapping

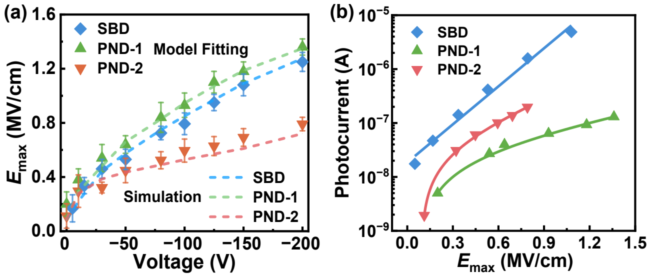

Fig. 8. (a) The obtained E_{max} from fitting and its comparison to the *E*-field values extracted from simulation (Error bars are calculated based on the standard error <0.07). (b) The relationship between the interfacial *E*-field and the photocurrent value from the photoresponse spectra at 266 nm.

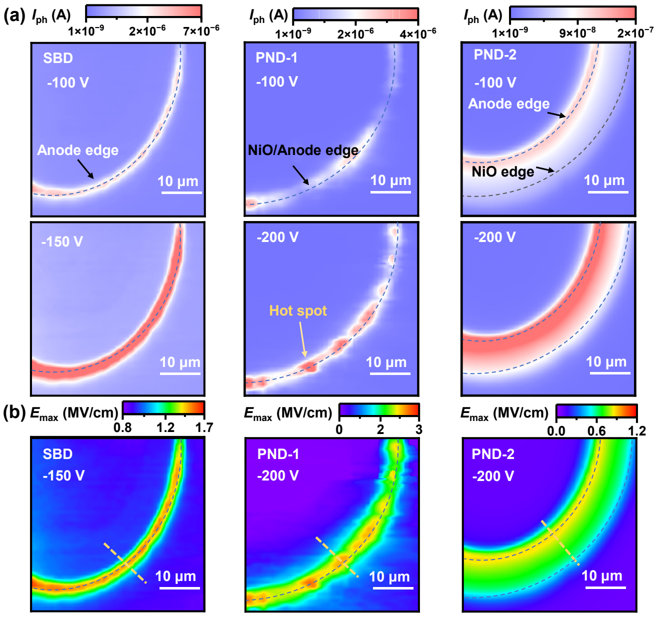

Fig. 9. (a) The photocurrent mapping spectra for three devices under two representative reverse biases up to 200 V. (b) 2-D maps of the interfacial *E*-field distributions within three devices at high reverse bias.

TCAD simulated and F-K mapped *E*-field Profiles

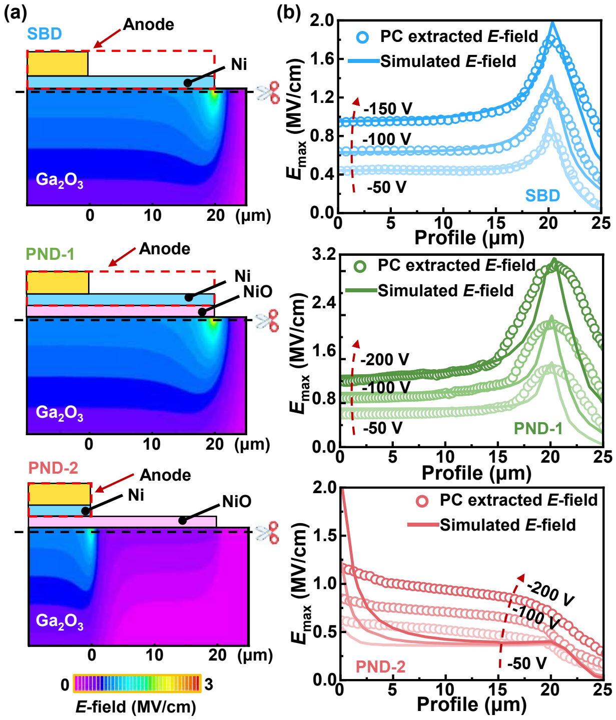

Fig. 10. (a) Simulated cross-sectional *E*-field contours in three devices. (b) The comparison between the simulated *E*-field (in solid lines) and the experimental *E*-field derived from photocurrent mapping (in hollow circles) along the cutline shown in Fig. 9, for all three devices each at three representative biases.

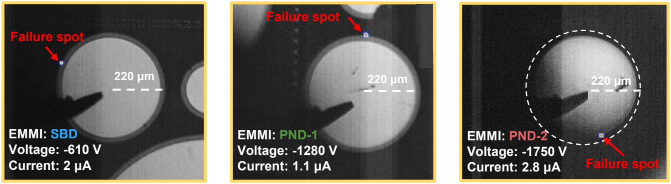

Fig. 11. Emission microscopy (EMMI) images of the killing leakage spots near the breakdown voltage of three devices. The locations of these failure spots are consistent with the peak *E*-field locations revealed in Figs. 9-10.

Benchmark

Table IV. Comparison of mechanism, performance, and applicability of our method and previously reported methods for *E*-field detection.

Reference	Method	Mechanism	Test sample	Performance				Applicability			
				Detection range	Applied voltage	Spatial Resolution	Intrusion	High voltage device	Dimension	In-operanto detection	Other limitations
[10]	Kelvin probe force microscopy	Electrostatic interaction with offset voltage	AlGaN/GaN	Several kV/cm	Low bias	Nanoscale (< 50 nm)	No	No	Surface 2D	Yes	Conductive sample
[11]	Liquid crystal electrography	Field-dependent orientation and opticity of liquid crystal	AlGaN/GaN	< 10 kV/cm	Low bias	0.5 μm	Yes	No	Surface 2D	Yes	Transparent device
[2]	NV centers	Single electron spin	Diamond	350 kV/cm	0 to 150 V	10 nm	Yes	Yes	Internal 2D	Yes	Materials that easily accommodates NV centers like diamond
[3]	EFISHG	Electric field interaction between two incident photons and external bias	GaN	Reach MV/cm	0 to 120 V	Submicron	No	Yes	Internal 2D	Yes	Nonlinear susceptibility and material symmetry
[1]	PR and CER	Reflectance oscillation	GaN	< 100 kV/cm	Low bias	-	No	No	-	Yes	Reflectance oscillations decay under high fields
[12]	Micro-Raman spectroscopy	Laser stimulated temperature-dependent phonon frequency	AlGaN/GaN	1.9 MV/cm	0 to 75 V	Submicron	No	No	Surface 2D	Yes	Detection under on-state and regions without metal contacts
This work	Photocurrent spectroscopy	Franz–Keldysh effect	UWBG-Ga_2O_3	0.1-3.1 MV/cm	0 to -200 V	Submicron	No	Yes	Internal 2D	Yes	Light penetrable surface